

Contents lists available at ScienceDirect

Carbon

journal homepage: www.elsevier.com/locate/carbon



Mechanistic understanding of Li metal anode processes in a model 3D conductive host based on vertically aligned carbon nanofibers

Sabari Rajendran, Archana Sekar, Jun Li*

Department of Chemistry, Kansas State University, Manhattan, KS, 66506, United States

ARTICLE INFO

Article history: Received 6 April 2023 Received in revised form 24 May 2023 Accepted 26 May 2023

Keywords:
Lithium metal anodes
3D lithiophilic conductive hosts
Vertically aligned carbon nanofiber arrays
Solid electrolyte interphase
Reversible lithium plating/stripping

ABSTRACT

The use of three dimensional (3D) conductive hosts is a promising strategy to alleviate dendrite formation in lithium metal anodes. However, the fundamental issues associated with the 3D hosts, such as formation of excessive solid electrolyte interphase (SEI) and complicated Li deposition morphologies, have not been well studied. This study focuses on understanding these critical issues using vertically aligned carbon nanofiber (VACNF) array as a model 3D host. Various characterization tools are employed to elucidate the morphology and composition of electrodeposited Li (e-Li) and its associated SEI. The e-Li on VACNFs exhibits two different morphologies – a dominant micron-scale columnar infiltrative Li and a small amount of nanoscale coaxial Li sheath on VACNFs in the unfilled interstitial area between infiltrative grains. During Li intercalation, an organic-rich loose SEI film forms on the top of VACNF array and an inorganic-rich SEI sheath forms around individual VACNFs. Li plating transforms them into inorganic dominant SEIs directly in contact with the e-Li surface. The SEI skins on the infiltrative Li remain loosely attached to the VACNF array after stripping Li and irreversibly accumulate during Li plating/stripping cycling, while the coaxial SEI on the nanoscale Li remains as a stable elastic sheath. The loose SEI skins cause electrolyte consumption and increased heterogeneity, eventually leading to cell failure.

© 20XX

1. Introduction

The ever-increasing global energy demand drives the need for the development of new battery technologies with higher energy density than the commercially available lithium-ion batteries (LIBs). Some of the promising candidates for the next generation batteries include lithium-sulfur and lithium-air batteries as they offer theoretical energy densities of 2567 Wh/kg and 3505 Wh/kg, respectively [1]. Both battery chemistries use lithium as the anode material. Lithium metal anode (LMA) is considered as the "holy grail" among various anode materials due to its highest theoretical capacity (3860 mAh/g) and its lowest redox potential (-3.04 V vs standard hydrogen electrode) [2,3]. Though LMA possesses these desired theoretical properties, the heterogeneous nature of lithium plating and stripping results in problems such as unstable solid electrolyte interphase (SEI), formation of lithium dendrites and electrically isolated dead Li [3-6]. Also being a hostless anode, lithium plating involves a virtually infinite volume expansion. All these result in poor coulombic efficiency (CE), loss of active Li, and poor cycling life, which hinder the commercialization of LMA. Solving these issues associated with LMA is essential in developing next generation batteries.

The formation of lithium dendrites is a serious concern as they pose a risk of creating an internal short-circuit by penetrating through the separator and reaching the cathode [7]. Besides inducing a sudden failure, the short-circuit easily causes fire due to the use of flammable electrolytes. Approaches commonly explored to prevent dendrites include use of three-dimensional (3D) conductive hosts as current collectors, addition of electrolyte additives, application of artificial SEIs, and use of solid-state electrolytes [8–12]. Among these, 3D conductive hosts suppress the formation of dendrites by extending the time for depleting Li⁺ ions on the anode surface during Li plating, owing to the reduction in the local current density. It is also claimed that 3D hosts homogenize the electric field to facilitate uniform plating [8,13]. In addition to these, the lower local current density is beneficial for more uniform stripping that prevents formation of dead lithium [14]. The rigidity and porosity of 3D hosts offer preserved rooms to accommodate the continuous Li plating/stripping during cycling without causing electrode volume changes.

Common 3D conductive host materials include copper, carbon, metal alloys, etc. [15]. Carbon based 3D hosts are favorable due to their high tunability in size, structure and chemical properties [16]. However, common carbon materials are inherently lithiophobic and hence require heteroatom doping or surface coatings with lithiophilic materials (such as ZnO, Ag, etc.) to serve as an effective host for LMA [17,18]. Though the host surface can be rendered lithiophilic, common 3D carbon hosts such as carbon cloth, carbon paper, etc., possess high tortuos-

* Corresponding author.

E-mail address: junli@ksu.edu (J. Li).

https://doi.org/10.1016/j.carbon.2023.118174 0008-6223/© 20XX ity which decreases Li+ diffusivity and impairs the complete utilization of available pore volume [19-21]. Also, it is important to have a low tortuous structure to avoid uneven filling of the pore volume [22]. On these aspects, several studies have successfully developed lithiophilic 3D carbon materials as hosts for high performance LMAs [20,23,24]. Lin et al. designed a composite material to store Li metal between the reduced graphene oxide (rGO) layers. The layered Li-rGO composite exhibited a smooth surface without formation of dendrites for 100 cycles [25], but the structure of the SEI on the internal surface of rGO layers during lithiation/delithiation processes was unknown. Similarly, in the study by Fang et al., Ag nanoparticle-embedded nitrogen-doped carbon macroporous fibers were used as the host material to achieve more than 500 cycles with the CE higher than 98% at 1 mA/cm². The improvement in performance was attributed to the lithiophilic nitrogen-doped carbon sites and functional Ag nanoparticles, which acted as nucleation sites for Li plating, while the macroporous framework mitigated the volume variation during cycling [20]. From the scanning electron microscopy (SEM) and transmission electron microscopy (TEM) images, it can be observed that Li growth occurred within the hollow spaces as well as on the outer surface of the fibers. It is noteworthy that, at high capacities, globules formed on the surface. Though the 3D hosts help to achieve a more stable cycling of LMA by preventing dendrite formation, it is not clear whether other issues, such as continuous formation of SEI and dead Li, still limit the performance. Huan Li et al., employed in-situ Raman to understand the lithium nucleation behavior in low surface area defective graphene electrodes. They found that, with the use of high surface area electrode, the cell failed due to electrolyte consumption [26]. However, they did not provide a good mechanistical understanding of the structure and nature of the innate SEI on the 3D material. It needs to be emphasized that, in addition to Li plating and stripping, Li intercalation and deintercalation processes could also occur in carbon based 3D hosts [13,27]. The unanswered fundamental scientific questions include where the SEI forms and its nature, what happens to the SEI at increased Li plating capacity, and what happens to the carbon host during the Li intercalation and plating, etc. These are crucial for designing better 3D host architectures for LMA.

In a previous study, we demonstrated that vertically aligned carbon nanofiber (VACNF) arrays, with a unique internal microstructure consisting of conically stacked graphitic cups, can serve as a low-tortuosity brush-like conductive 3D carbon host for high-performance LMAs [13]. In this study, we have chosen VACNFs grown on Cu substrate (VACNF/ Cu) as the 3D host to understand the critical processes involved in LMA. The following characteristics of VACNF arrays make it an ideal model to answer the aforementioned fundamental questions. VACNFs are graphitic carbon inherently doped with nitrogen atoms and functionalized with oxygenated groups at the sidewalls, rendering them more lithiophilic comparing to other 3D carbon hosts [13]. While other carbonaceous 3D hosts require additional processes to dope heteroatoms or coat lithiophilic materials. The high aspect ratio of VACNFs provides a large surface area while their vertical alignment and open pore structure (~80% porosity) offer short and low tortuous pathways for fast and uniform Li⁺ ions diffusion throughout the whole electrode [28-30]. This differs from other 3D hosts based on carbon cloth and carbon paper consist of micron-sized or nano-sized carbon fibers stacked horizontally with a wide range of pore sizes from a few microns to tens of microns [19,20]. Most of the 3D hosts are quite thick with poorly defined pore structure and high tortuosity resulting in non-uniform filling of Li which impedes the complete utilization of pore volume [31]. The high surface area of these hosts relies on their large thicknesses which would decrease the volume-specific capacity of the 3D LMAs. In contrast, VACNF/Cu is designed such that the entire pore volume would be utilized for the capacity being tested. The VACNFs can be easily scraped off from the copper substrate and transferred to TEM grids, making it possible to evaluate the details of SEI and Li plating on individual VAC-NFs. This was difficult with common carbon host structures. In brief,

the stark contrast between VACNFs and other 3D hosts lies in its well-defined, aligned pore structure with inherent lithiophilic nature which makes it a less complicated 3D host structure, serving as a good model system of LMA hosts.

In this report, we employ various characterization techniques such as in-situ Raman microscopy, X-ray photoelectron spectroscopy (XPS) depth profiling, cryo-TEM, field-emission SEM (FESEM) to gain deeper understanding on the structure, composition and dynamics of SEI, Li intercalation/deintercalation, and Li plating/stripping in VACNF arrays. These studies are correlated with the enhanced electrochemical performance using VACNF arrays as a 3D LMA host. Interestingly, both SEI and electrodeposited Li are highly heterogeneous over a wide length scale. Two types of SEIs, on top of the VACNF array and around individual VACNFs, are formed during intercalation process, which are further reduced into more compact SEIs during Li plating. The morphology of electrodeposited lithium (e-Li) is composed of micron-scale columnar Li grains infiltrated into VACNF arrays and nanoscale coaxial Li sheath wrapped around individual VACNFs in the interstitial area between the columnar Li grains. They behave differently during Li stripping. The 3D structured host reduces the irreversible SEI formation and electrolyte consumption compared to planar Cu electrode but cannot eliminate them. These critical factors provide useful insights to develop future solutions to further enhance the performance of LMAs.

2. Materials and methods

2.1. Chemicals and materials

Electrolyte solution containing 1.0 M lithium bis(trifluoromethane-sulfonyl)imide (LiTFSI) in 1,3-dioxolane (DOL) and 1,2-dimethoxyethane (DME) (1:1, $\rm v/v$) with 1 wt % LiNO $_{\rm 3}$ additive was purchased from Dodochem Limited (Suzhou, China). Copper foils (99.999%) were purchased from Fisher Scientific (Hampton, NH) and GoodFellow Corporation (Pittsburgh, PA). Li foil, CR2032 coin cell casings, spacers, and wave springs were purchased from MTI Corporation (Richmond, CA). The separators Celgard 2400 and glass fiber discs were purchased from Celgard (Charlotte, NC) and El-Cell GmbH (Hamburg, Germany), respectively.

2.2. VACNF/Cu electrode preparation

An 84 μm thick copper foil was used as the substrate for the growth of VACNFs. A 300 nm thick Cr barrier layer and a 30 nm thick Ni catalyst layer were sputter coated using a high-vacuum PerkinElmer 4400 series magnetron sputtering system at UHV Sputtering Inc. (Morgan Hill, CA). VACNFs were grown using a DC biased plasma enhanced chemical vapor deposition (PECVD) unit (Black Magic, Aixtron, CA) following the same procedure reported in previous studies [13,29,32]. In brief, the substrate was heated to 500 °C at a rate of 200 °C/min with ammonia gas at a flow rate of 250 sccm, at a pressure of 3.9 Torr. Under these conditions, a DC plasma at 40 W was applied for 60 s to dewet and break the Ni film into randomly distributed Ni nanoparticles. Then, the temperature was increased to 750 °C at a rate of 250 °C/min while 70 sccm acetylene gas was introduced as the carbon precursor along with the ammonia gas to give a steady-state pressure of 4.8 Torr. The process was continued for 90 min to grow 15 μm long VACNFs on Cu.

2.3. Materials characterization

The morphology of the electrodes was studied using Topcon/ISI/ABT DS 130F FESEM (Akashi Beam Technology Corporation, Tokyo, Japan) and Helios NanoLab 660 (FEI, OR) with a focused ion beam (FIB) milling functionality. To image intercalated and/or electroplated lithium on VACNF/Cu hosts, the electrodes were harvested from half-cells by disassembling in an Ar-filled glovebox. The harvested elec-

trodes were washed by immersing in DME several times. After drying in the antechamber of glovebox under vacuum, FESEM samples were prepared back in the glovebox. The prepared samples were then stored in a tightly sealed container filled with ultrapure Ar. The samples were exposed to ambient air for a few seconds during transferring from the sealed container to the sample stage. Before FIB milling, a 2 μm thick Pt layer was deposited to protect the underneath structure from ion beam damage. An ECC-Opto-Std optical cell (El-Cell GmbH, Hamburg, Germany) was used for in-situ Raman experiments. A glass fiber separator (El-Cell GmbH, Hamburg, Germany) of 0.65 mm thickness and 10 mm diameter was used. The VACNF/Cu and Li foil electrodes of 3.0 mm wide and 15.0 mm long were placed side by side on top of the glass fiber separator. The optical cell was filled with 1.0 M LiTFSI in DOL and DME (1:1, v/v) with 1 wt% LiNO₃ electrolyte. A constant current of 10 μA was applied for Li intercalation/deintercalation cycles while the cell voltage was varied between 0.0 and 1.0 V (vs Li+/Li). For lithium plating, 10 µA was employed for a duration of 13 h. Lithium stripping was carried out at the same current till the voltage reached 1.0 V (vs Li+/Li). Raman spectra were acquired using a DXR Raman microscope (Thermo Fisher Scientific, Madison, WI) with a 532 nm laser at a power of 10 mW, using a 10Xobjective lens with a slit width of 25 µm at different electrode potentials while cycling. A total of 16 exposures for a duration of 10 s per exposure was used. XPS depth profiling was carried out using a PHI 5000 Versa XPS system (Chanhassen, MN) with a monochromatized Al Kα source (1486.7 eV) with a 400 μm spot size. Samples were prepared according to the sample preparation procedure followed for FESEM imaging. Shirley background was used for XPS analysis. The C 1s peak at 284.60 eV was used as the standard to calibrate all XPS spectra. The morphology of individual VACNFs was imaged using a Philips CM 100 TEM at a 100 kV acceleration voltage in low dose mode at -175 °C using a Gatan cryo-holder. The VACNFs were transferred to TEM grids by scraping them from the electrode inside a glovebox. The TEM grids were stored in Ar filled storage holders and plunged in liquid nitrogen without exposing to air. This was followed by transfer of the TEM grid to the cryo-holder using a cryo-station. The cryo-shield was used to prevent the sample from exposure to the air during the transfer from cryo-station to TEM.

2.4. Electrochemical characterization

VACNF/Cu or planar Cu foil electrodes of 15 mm in diameter were used as the working electrode to assemble half-cells using CR2032 casings. A 25 μm thick Celgard 2400 and a 0.65 mm thick Li foil were used as the separator and counter electrode, respectively. A 0.3 mm thick stainless steel wave spring and two pieces of 0.2 mm thick stainlesssteel spacers were used to provide consistent pressure and good contact between the components. The Li foils were polished using 200 and 400 grit sandpapers before assembling. 250 μ L of 1.0 M LiTFSI in DOL/DME (1:1, v/v) solvent with 1 wt% LiNO3 additive was used as the electrolyte in the flooded condition. The half-cells were assembled in an argon-filled glovebox (Mbraun MB10 Compact, Stratham, NH) with oxygen and water levels below 0.5 ppm. The assembled half-cells were tested using a battery testing system (Neware, Shenzhen, China) at room temperature. Five cycles of Li intercalation/deintercalation at $50 \,\mu\text{A}$ were done between $0.0 \,\text{V}$ and $1.0 \,\text{V}$ (vs Li⁺/Li) before Li plating. Li plating and stripping processes were conducted by applying a constant current density of 1.0 mA/cm2 to obtain desired capacities. For the CE test, a capacity of 2.0 mAh/cm² was employed. The upper cut-off voltage for Li stripping was 1.0 V vs Li+/Li. The CE was calculated as the ratio of Li stripping capacity to Li plating capacity, expressed in units of percentage. The symmetric cycling measurement was done with coin cells with a working electrode (VACNF/Cu or planar Cu) vs. a Li disk counter electrode at 1.0 mA/cm² with a cycling capacity of 1.0 mAh/cm². Prior to symmetric cycling, the working electrodes were cycled at 1.0 mA/cm² up to 2.0 mAh/cm² capacity for three times followed by plating 2.0 mAh/cm² of stablized Li for further experiments.

3. Results and discussion

3.1. Materials and electrochemical characterization of VACNF/Cu electrode

Firstly, the structure and chemical composition of pristine VACNF/ Cu, the chosen model LMA host for this study, was carefully characterized. The FESEM images of the VACNF grown on Cu substrate for 90 min are shown in Fig. 1a-c and Figs. S1a&b. As seen at a 30° perspective view, the VACNFs form an array with rather uniform vertical alignment. A scratch was purposely made on the VACNF array in Fig. 1a so that their length can be viewed at the cross-section. From the top-view images (Fig. 1c and Fig. S1b), the VACNFs are highly aligned perpendicular to the surface of the Cu substrate. Per the calculation shown in Fig. S1c, the porosity was found to be ~78.6%. The average length and diameter of the VACNFs were determined to be ~14 µm and ~154 nm, respectively. A histogram of the fiber diameter is shown in Fig. S2, which is defined by the diameter of the Ni catalyst particle at the tip of each VACNF. TEM and HRTEM images of VACNF (Fig. 1d and Fig. S3) illustrate the conically stacked graphitic cups with an abundance of graphitic edges on the surface of sidewalls. Since the VACNFs grew by the tip growth mode, the inverse tear drop shaped Ni catalyst retained at the tip of the VACNF and was covered by a thin layer (~2-4 nm) of carbon. This was validated by the XPS data (Fig. S4) which confirmed the presence of Ni within a depth of 2-10 nm from the surface. The XPS results (Fig. S5) also revealed that the VACNFs were doped with 2.9% of oxygen and 7.3% of nitrogen, respectively. The N 1s peak can be deconvoluted into four peaks with the binding energies (BEs) at 396.3, 398.4, 400.5, and 402.5 eV, corresponding to pyridinic N, pyrrolic N, graphitic N, and pyridinic N oxide, respectively. The O 1s peak was deconvoluted into four components with BEs at 531.2, 532.2, 533.4, and 535.1 eV corresponding to C-O, C=O in carboxylic group (-COOH), -OH group and adsorbed water, respectively. To understand the location of dopants, the top surface of pristine VACNF array was etched using Ar+ at a rate of 0.08 nm/s for 60 s. This translates to removal of ~4.8 nm thick materials, which is equivalent to ~14 layers of graphitic planes. As shown in Fig. S5, after etching, the O at% decreased by 69% to a total of 0.9%. Meanwhile, N at% slightly decreased to 7.0%. However, the composition of the N doping changed as follows. The amount of pyridinic N oxide decreased significantly by about 53% and those of pyridinic N and pyrrolic N increased by 54% and 25%, respectively, while that of graphitic N did not change much. The significant decrease in oxygen and pyridinic N oxide indicates that oxygenated functional groups are present only on the exposed edges of VACNFs. After etching off the surface, the pyridinic N and pyrrolic N groups located within the few layers from the surface would also get removed but those located deeper will get exposed. Also, during the etching, graphitic nitrogen situated close to the surface may get converted to pyridinic/pyrrolic N. Due to the absence of oxygen during the etching process, pyridinic N oxides are not formed. This proves that nitrogen dopants are present throughout the structure of VACNFs while oxygen functional groups are present only at the graphitic edges.

Half-cells were constructed with VACNF/Cu and planar Cu electrodes as working electrodes to evaluate their performance as LMA hosts. The CE was assessed at $1.0~\text{mA/cm}^2$ with a cycling capacity of $2.0~\text{mAh/cm}^2$, based on our previous work that filling the entire pore volume of VACNF/Cu with Li would yield a plating capacity of $2.0~\text{mAh/cm}^2$. As shown in Fig. 1e, the CE for VACNF/Cu was only around 87.8% in the first cycle, owing to the formation of initial SEI and the intercalation of Li⁺ ions into the graphitic structure of VACNFs. From the second cycle, the CE was stabilized at \sim 98% and retained at this level for about 130 cycles. In the case of planar Cu, the cell was only stable

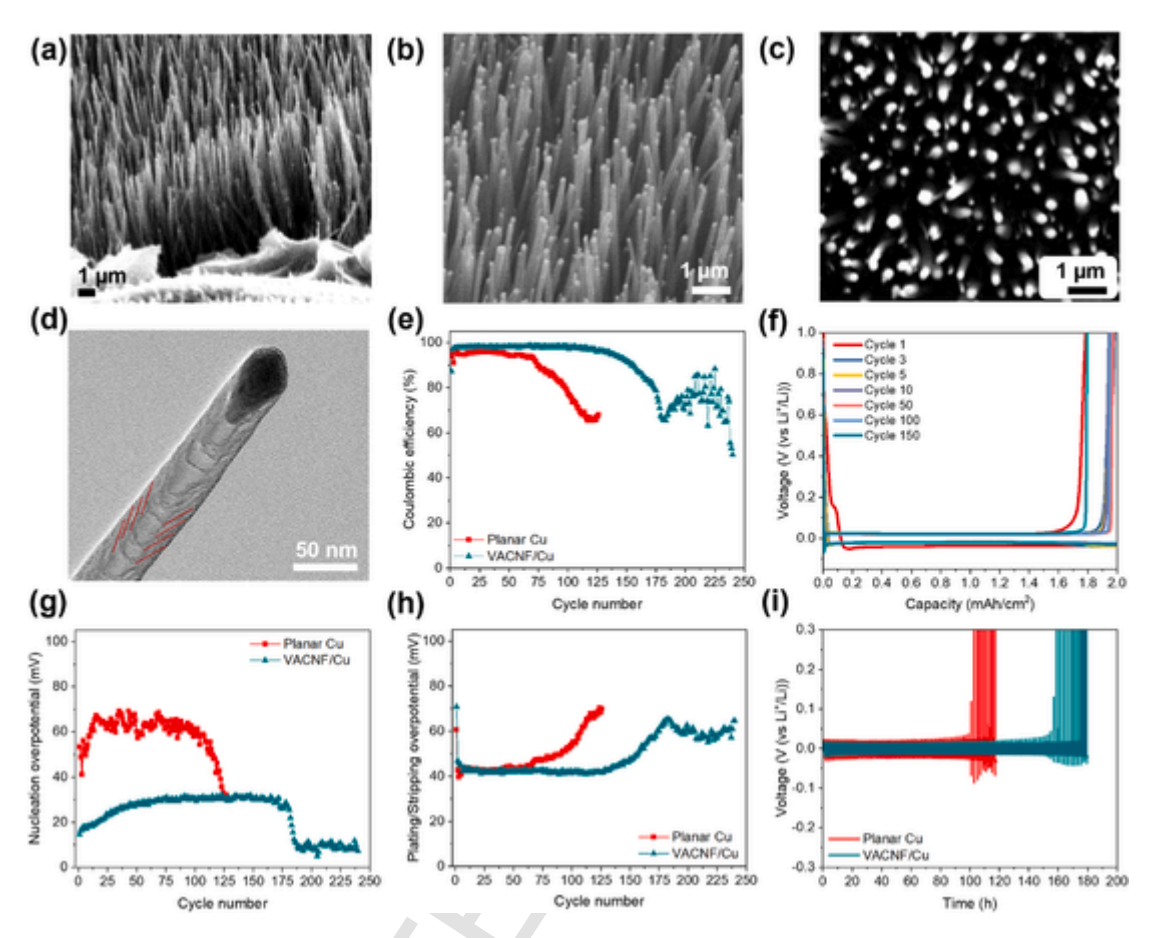


Fig. 1. FESEM images of VACNF grown on Cu substrate at (a), (b) a 30° perspective view, and (c) a 0° top view. (d) TEM image of a VACNF. (e) CE during Li plating/stripping cycling with 2.0 mAh/cm² capacity at 1.0 mA/cm² for VACNF/Cu and planar Cu electrodes, respectively. (f) Voltage curves for Li plating/stripping on a VACNF/Cu electrode at different cycles. Evolution of (g) Li nucleation overpotential and (h) Li plating/stripping overpotential over cycles shown in (e). (i) Symmetric cycling performance of VACNF/Cu and planar Cu electrodes, respectively, plated with 2.0 mAh/cm² Li at a cycling capacity of 1.0 mAh/cm² and a current density of 1.0 mA/cm². (A colour version of this figure can be viewed online.)

for about 44 cycles with a lower average CE of 95.4%. The higher CE and longer cycle life of VACNF/Cu than the planar Cu make the advantages of using 3D hosts for LMA quite evident, which are supported by the recent studies [33,34]. The capacity associated with Li intercalation into VACNFs and SEI formation were significantly reduced in cycle #2-5, as shown in the Li plating voltage curves in Fig. 1f and S6. In the first cycle, a capacity of about 0.05-0.07 mAh/cm² was consumed in the potential range of 0.2–0.0 V (vs Li⁺/Li). This can be attributed to lithium intercalation into VACNFs, translating to a specific capacity of 84-117 mAh/g_{VACNF} which is only 22-31% of theoretical capacity of graphite. Hence, only a small portion of graphitic carbon in VACNFs (likely only at the exterior surface) is intercalated with Li+ at 1.0 mA/cm² current density (the typical rate where Li plating is done in later discussion). Even at a lower current of 0.028 mA/cm², the lithiation capacity was ${\sim}150~\text{mAh/g}_{\text{VACNF}}$ (${\sim}40\%$ of the theoretical capacity of graphite) as shown in Fig. S7. This small Li intercalation is helpful to make VACNFs lithiophilic before Li plating starts while maintaining their structural integrity. After stable cycling for ~130 cycles, the CE of VACNF/Cu started to decline continuously to a minimal value of 66% in the 182nd cycle. Beyond this point, the CE increased from 66% to 78% (in the 200th cycle) and then became very unstable. The planar Cu foil electrode showed a similar behavior but with a much shorter life. The behavior of increasing CE towards the end of cycle life could be due to reattachment of physically isolated lithium particles that resulted in increased stripping capacity [35,36]. Whether the use of VACNFs as 3D conductive wires improves the chances of reattachment of dead Li is an interesting topic of future studies.

The Li plating/stripping overpotential (η_{ps}) and the Li nucleation overpotential (η_{nuc}) were calculated as depicted in Fig. S8. In the stable cycles, VACNF/Cu and planar Cu had similar η_{ps} of ~40 mV (Fig. 1h), but showed distinct behavior in η_{nuc} (Fig. 1g). In the first cycle, VACNF/ Cu exhibited a lower η_{nuc} of 14.5 mV compared to that of planar Cu (53.4 mV). The lower nucleation overpotential for VACNF/Cu is due to the high surface area of VACNFs and the lithiophilic nature owing to graphitic edges, N and O doping, and Li intercalation. These factors collectively decreased the energy barrier for the Li nucleation process. In following cycles, the η_{nuc} of VACNF/Cu gradually increased and got stabilized at 30.1 mV (Fig. 1g). When the CE started to decline, the η_{nuc} quickly dropped to 8.1 mV, a value lower than the initial η_{nuc} . This trend was observed for planar Cu as well but in much earlier cycles. This could be an indicator for the growth of uncontrolled high-surfacearea Li structures and/or activation of unstripped lithium sites of previous cycles in the dynamic environment inside the coin cell, which facilitate Li nucleation. As shown in Fig. 1h, during this same period, the $\eta_{\rm ps}$ increased to ~65 mV for both electrodes, indicating accumulation of SEI/dead Li due to increased consumption of electrolyte during the end of cycle life [35]. This would lead to zones where electrolyte is deprived, making the electrode surface more heterogeneous and leaving behind a large amount of dead Li and SEI as indicated by the low CE. While it is well known that 3D conductive host, such as VACNF arrays, can improve the reversibility of Li plating/stripping (Table S1), it is important to understand the failure mechanism to gain insights into strategies for further improvement, which is the foci of this study.

Symmetric cell cycling was also performed to understand the stability of SEI and reversibility of Li plating/stripping. The cycling capacity was kept at 1.0 mAh/cm², i.e., 50% depth of discharge (DoD), at a rate of 1.0 mA/cm² using VACNF/Cu and Cu electrodes plated with 2.0 mAh/cm² vs a Li foil counter electrode. As shown in Fig. 1i, VACNF/Cu electrode exhibited a longer cycling life (156 h) when compared with planar Cu (100 h). This improvement in performance could be attributed to higher reversibility of Li plating/stripping and a more stable SEI formation in VACNF/Cu electrode. For both electrodes, the cells failed by an increase in the electrode potential due to unavailability of sufficient active Li to deliver the defined stripping capacity. Consistent with the previous report, VACNF/Cu is indeed a superior LMA host compared to planar Cu [13]. With the testing conditions employed in this study, no internal short circuits due to dendritic growth were observed. However, the electrochemical data indicates continuous consumption of electrolyte and active Li, consistent with recent literature [26,37,38]. Further characterization was carried out to shed light on the processes that occurred on VACNFs during the Li intercalation/deintercalation and Li plating/stripping.

3.2. Morphological analysis of electrodeposited Li using FESEM

To understand the morphology of electrodeposited Li (e-Li) on VACNF/Cu, FESEM images were taken after plating different capacities of Li at 1.0 mA/cm², as shown in Fig. 2a-f. After depositing a low capacity of about 0.75 mAh/cm² of Li, micron-scale particles of Li of an average size of 2.7 μm were observed (as the darker spots in Fig. 2a). The density of micron-scale Li particles was calculated to be about 5.6 \times 106 particles/cm². Fig. 2b-f revealed that the VACNF/Cu plated

with the full capacity of 2 mAh/cm² Li displayed two different morphologies - (i) micron-scale, pillar-like, columnar Li infiltrating the open spaces among the VACNFs (referred to as infiltrative e-Li), (ii) nanoscale Li that coaxially deposited on the surface of individual VAC-NFs (referred to as nanoscale e-Li) in the area between the micron-scale columnar grains. The columnar structure of infiltrative e-Li without pores are generally reported to be favorable for Li metal anodes as it reduces the active surface area, thereby decreasing the consumption of active Li and electrolyte due to irreversible SEI formation [39,40]. FIB-FESEM image (Fig. 2f) further showed that the infiltrative Li was nonporous in nature and it completely filled the pore volume among the VACNFs. The enhancement in reversibility/CE of Li plating/stripping on VACNF/Cu electrode could be attributed to this columnar Li morphology. VACNFs acted as conductive wires to maximize the electrical connection with the plated Li and reduced formation of dead Li. The growth of columnar Li in the unique low-tortuous open pore structure of VACNF arrays demonstrates the effectiveness of 3D structure on improving the e-Li morphology. Besides the micron-scale columnar infiltrative e-Li, nanoscale e-Li were observed on the VACNFs that were not engulfed by the infiltrative e-Li. The histogram analysis of the diameters of VACNFs after Li plating with different capacities and after Li stripping were analyzed as shown in Fig. S10. It revealed that the average fiber diameter increased from ~154 nm to ~163 nm after plating 0.75 mAh/cm². It further increased to about ~226 nm after an additional plating of 1.25 mAh/cm² Li. The increase in fiber diameter can be attributed to the coaxial sheath of nanoscale e-Li and the SEI. The sheath thicknesses was about 4.5 nm and 36 nm for Li capacity of 0.75 and 2.0 mAh/cm², respectively.

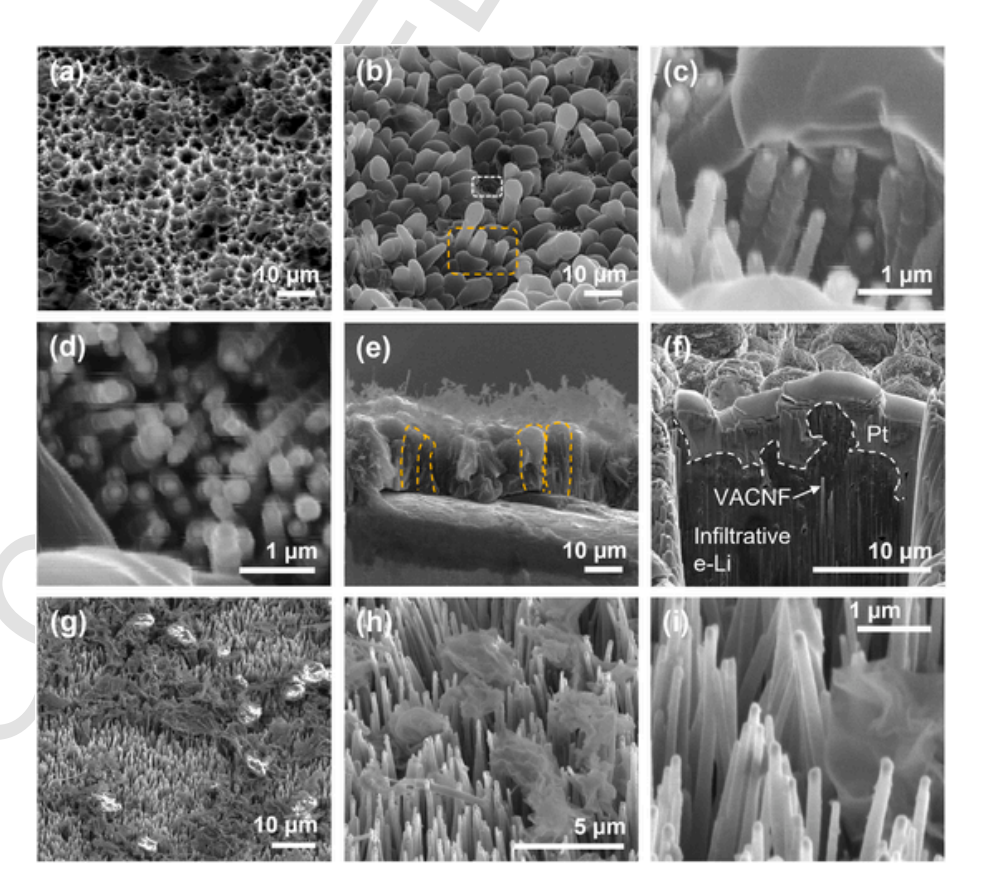


Fig. 2. FESEM images at 30° perspective view of VACNF/Cu electrodes after Li plating at 1.0 mA/cm² to the capacity of (a) 0.75 mAh/cm² and (b) 2.0 mAh/cm². (c) The FESEM images at 30° perspective view and (d) top view of the region highlighted using white dashed rectangle in panel b. (e) Cross-sectional and (f) FIB-milled cross-sectional FESEM images of VACNF/Cu plated with 2.0 mAh/cm² Li. A protective layer of 2 μm thick Pt layer was deposited on the top surface to protect the structure underneath from Ga⁺ ion beam damage as shown in Fig. S9. (g)–(i) FESEM images at 30° perspective view of Li-plated VACNF/Cu electrodes after completely stripping the 2.0 mAh/cm² plated Li at a rate of 1.0 mA/cm². (A colour version of this figure can be viewed online.)

After completely stripping Li from the fully plated VACNF/Cu (with 2.0 mAh/cm² capacity), the infiltrative e-Li was clearly removed, leaving behind only the soft SEI skins floating in the VACNF host (Fig. 2g-i). Contrary to the uniform SEI thin films on planar electrode surface, the SEI skins left off from infiltrative e-Li were of wrinkled 3D nature, wrapping around the bundle of VACNFs as shown in Fig. S11. This also offers additional evidence for the engulfing nature of infiltrative e-Li. It is quite surprising that most of the studies on 3D conductive hosts were not able to observe such stripped SEI skins even though their CE is less than 98% [20]. One of the possibilities is that most 3D conductive hosts were made of powder materials which had complicated tortuous composite structure. The SEI can be disrupted during the electrode preparation for SEM or TEM imaging. The open vertical architecture of VACNF array serves as a unique model to observe the plated Li and stripped SEI skins without disrupting the electrode structure.

As for the coaxially plated nanoscale e-Li, the sidewall of the VAC-NFs became smoother after completing Li stripping and their average diameter was reduced to 161 nm. The coaxial SEI sheath left behind by nanoscale e-Li is very thin and cannot be observed using FESEM. However, from the similar average diameter between the VACNFs after plating of 0.75 mAh/cm² Li and those after complete Li stripping, it can be concluded that, at the low plating capacity of 0.75 mAh/cm², only a small fraction of Li was plated as nanoscale e-Li sheath. With further plating, more Li was deposited as the nanoscale e-Li in the interstitial area of infiltrative e-Li particles. The high surface area of nanoscale e-Li would theoretically consume a greater amount of electrolyte if the SEI were to repeatedly form over cycles. However, considering the improved cycling performance of VACNF/Cu than planar Cu foil and the significant decrease in SEI capacity from second cycle during the activation process (i.e., the charging capacity in Fig. 1f and Fig. S6), the SEI

on the nanoscale e-Li likely remains as a stable elastic sheath during Li plating and stripping cycles.

In contrast to the e-Li morphology on VACNF arrays, the e-Li on planar Cu exhibited a very different morphology consisting of stacked spherical particles (as shown in Figs. S12a and S12b) consistent with literature [41,42]. The average size of the spherical particles was 2.1 μm after plating 0.75 mAh/cm² of Li. The presence of whisker-like/dendritic Li was also observed (pointed by yellow arrows in Fig. S12c). After stripping Li, abundant SEI skins shed from Li particles were left on the surface of planar Cu (Figs. S12d and S12e). Also, dead dendritic Li were present as indicated in Fig. S12f. Without having any structural support as in VACNF/Cu, there is a greater amount of dead Li as well as dendritic Li [43]. This microscopic observation correlates well with the lower CE and shorter cycle life of planar Cu electrodes.

3.3. In-situ Raman spectroscopic analysis

Since Raman spectroscopy is a proven characterization tool for studying carbon-based structures, we applied it for in-situ study of the changes in VACNFs during Li intercalation/deintercalation and Li plating/stripping processes. The experiments were performed using a commercially available optical cell from El-cell with a sapphire window for the laser probe. A side-by-side configuration (Fig. 3a) was found to be the optimal setup with minimal background signal from electrolyte while proper electrochemical control can be applied (as discussed below Fig. S14 of the SI). It is to be noted that a potential gradient exists across the electrode surface in this configuration. To minimize this effect, a low current of $10\,\mu\text{A}$ was used to allow sufficient time for the Li+ion diffusion. Normal charge-discharge curves could be obtained, and the measurements were made at designated points in Fig. 3b without

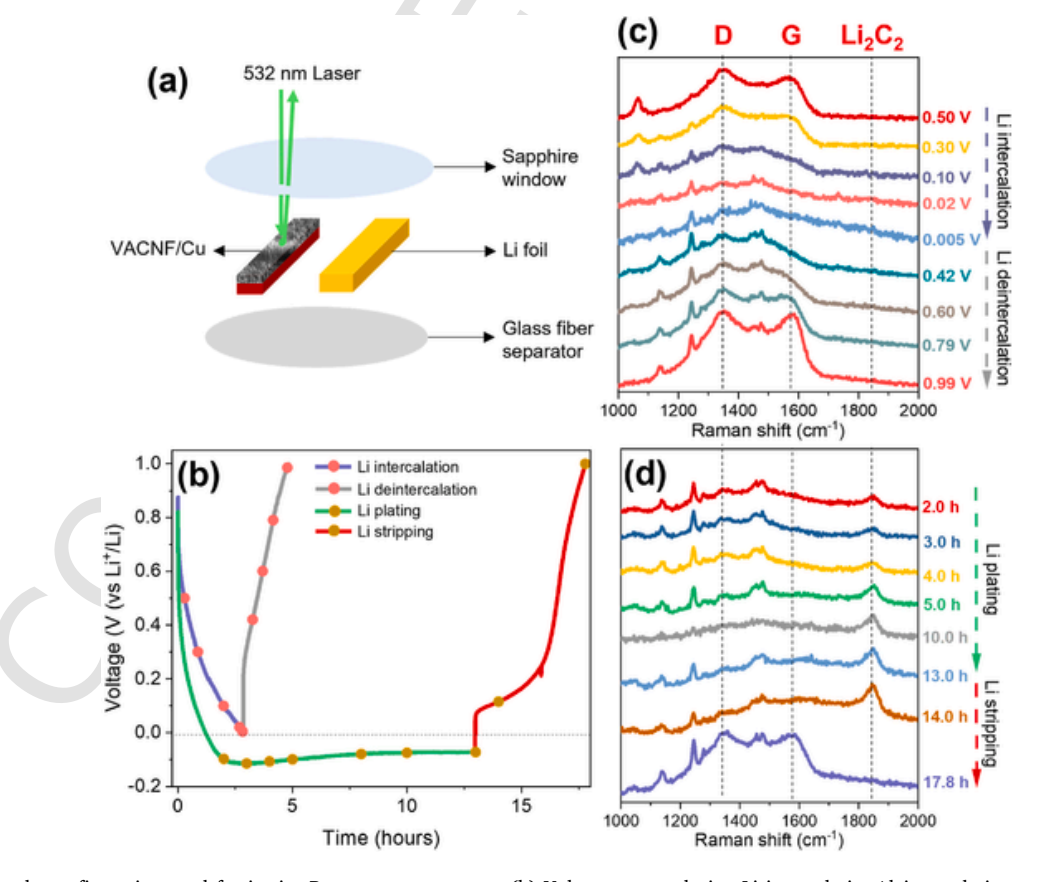


Fig. 3. (a) Electrode configuration used for in-situ Raman measurements. (b) Voltage curves during Li intercalation/deintercalation and Li plating/stripping at 10μ A for VACNF/Cu electrode during in-situ Raman measurements. In-situ Raman spectra of VACNF/Cu electrode (c) taken around the voltages highlighted as solid pink circles in panel b during Li intercalation/deintercalation and (d) taken around the designated time highlighted as solid yellow circles during Li plating/stripping processes. The Raman spectra were collected during the cycling without interrupting the cycling. (A colour version of this figure can be viewed online.)

disrupting the processes. The Raman spectrum of the pristine VACNF in Fig. S13 showed the characteristic Raman bands at $\sim\!1350~\text{cm}^{-1}$ and $\sim\!1550~\text{cm}^{-1}$ corresponding to D and G bands of graphitic carbon, respectively. The D band is associated with the vibrational modes of carbon atoms in defect sites and edges of the graphitic planes while the G band is attributed to the vibrations of sp² hybridized carbon atoms in the graphitic planes. Their intensity ratio (I_D/I_G) is an indicator of the defect density in graphitic carbon materials. For pristine VACNFs, the I_D/I_G ratio was 0.92. The high I_D in VACNFs is due to the abundance of graphitic edges and the defect sites doped with nitrogen and oxygen functional groups.

First, the VACNF/Cu electrode was lithiated/delithiated by cycling between 1.0 V and 0.0 V vs Li+/Li in which range no Li plating occurred. Fig. 3c shows the changes in the characteristic D and G bands of VACNFs during Li intercalation and deintercalation. Additional data are reported in Fig. S15. For the laser focal size of 2 μ m, it collects signals from about 30 to 60 VACNFs and the electrolyte filled within the open spaces among VACNFs. Hence, the Raman spectra included the bands corresponding to the VACNFs as well as a set of sharp bands from the electrolyte (Fig. S16). Like other researchers, we were unsuccessful in detecting the components of SEI such as Li₂O, Li₂CO₃, etc. [44]. Even though these materials are Raman active, the signal is too weak due to their nanoscale nature. Hence our foci are the D and G bands which clearly decreased and finally disappeared upon Li intercalation. Interestingly, during Li deintercalation, they reappeared without significant change in the band shapes from pristine VACNFs. This is an indication of reversible Li intercalation and deintercalation without structural damage. This reversible phenomena of Li intercalation/deintercalation were repeated for several cycles. The complete disappearance of D and G bands confirms that Li intercalation compounds formed in VACNFs which caused strong light absorption and reduced the depth from which the Raman scattering may occur [45]. The disappearance of G band can be also attributed to the Pauli blocking of interband optical transition preventing resonant Raman process [46]. The formation of lithium intercalation compounds on the surface of VACNFs before lithium plating is beneficial as it further improves the lithiophilicity and electronic conductivity [47].

However, the changes in D & G bands versus the degree of lithiation were quite different from that of graphite particles. In case of pure graphite, the G band changes before the D band, which shifts initially, broadens, splits into two and finally disappears during lithiation [45]. For other defective carbon materials, D bands disappear first and reappear later attributed to preference of Li+ toward defect sites [26]. For VACNFs, the D band disappeared later and reappeared earlier than the G band. As from the earlier estimation, the lithiation capacity of VAC-NFs is rather low (30%-40%). It was also observed that the color of lithiated VACNF remained black/grey (Fig. S17a) while fully lithiated graphite (LiC₆) is golden yellow [48]. Both in-situ Raman study (Fig. 3 and Fig. S15) and FESEM characterization (Figs. S17b and S17c) demonstrated that VACNFs undergo reversible lithiation and delithiation, likely involving only a thin layer at the sidewall surface of VAC-NFs, which does not damage their inherent structure. Since the defect sites located deeper within the VACNFs might not be available compared to sp² carbons on the outer portions, the Li intercalation caused the G band to disappear earlier than the D band. This corroborates with the early revelation by XPS that N atoms are rather uniformly doped inside VACNFs while oxygenated functional groups only present at the exposed edges at the exterior sidewall surface. Other techniques such as operando XRD, in-situ cryo-TEM, and DFT studies might be able to provide more insights into the lithium intercalation mechanism.

Next, the lower voltage limit at 0 V was removed to allow Li plating/stripping cycling at 10 μ A current while Raman spectra were collected (Fig. 3d and Fig. S18). As the cell voltage decreased to 0 V, similar changes in the D and G bands to those during Li intercalation/deintercalation cycles were observed. When the cell voltage was further re-

duced to negative values, a new band appeared at ~1850 cm⁻¹. This band can be attributed to lithium acetylide/carbide (Li₂C₂) which formed through reactions of Li with pre-existing SEI or electrolyte [44]. It is reported that Li₂C₂ is a component of SEI [49]. The origin of this band is due to the surface enhanced Raman scattering (SERS) effect of nanoscale e-Li on individual VACNFs [44]. With further Li plating, the intensity of Li₂C₂ peak increased indicating the growth of nanoscale e-Li. The FESEM images (Fig. 2c-d) clearly show that their size remains in the nanoscale range even after plating 2.0 mAh/cm². When the plated lithium was stripped off, the Li₂C₂ band vanished completely along with the reappearance of D and G bands of VACNFs. The vanishing of Li₂C₂ band can be attributed to complete stripping of nanoscale e-Li and loss of the SERS effect while Li2C2 remained in the SEI. Thus, Li2C2 band serves as a good indicator of the formation of nanoscale e-Li. To the best of our knowledge, this is the first in-situ Raman observation of reversible formation and stripping of nanoscale Li in 3D hosts using lithium acetylide/carbide as an indicator. It would be interesting to study further whether this can be used to reveal the presence of dead Li and Li dendrites in nanoscale regime using micro-Raman imaging.

3.4. Chemical and structural analysis of SEI

3.4.1. XPS depth profiling

XPS depth profiling based on Ar⁺ ion etching for different time periods was employed to understand the chemical composition of the SEI formed on Li-intercalated VACNFs (Fig. 4 and Fig. S19). Interestingly, after Li intercalation, Ni 2p signals were absent. For pristine VACNFs, as stated earlier, the ability to observe Ni 2p peaks makes it a good internal reference for the position of VACNF tips while performing depth analysis. This confirms the presence of a SEI layer on top of the VACNF array (see Fig. 4a) with a thickness greater than the sampling depth of XPS. Deconvolution of the C 1s peak showed the existence of five different C atoms. The deconvoluted peaks at 282.7, 284.6, 286.5, 288.6, and 290.0 eV can be assigned to carbide (-C=C-), alkyl or aliphatic groups (C-C/C-H), alkoxy groups (C-OR), carboxyl groups (R-COO) and carbonates (CO₃²⁻), respectively, with the alkyl or aliphatic groups (C-C/C-H) being the dominant one. The F 1s peak was deconvoluted into two peaks at 688.5 and 684.9 eV corresponding to -CF_x and LiF, respectively. The decomposition of the salt LiTFSI resulted in the formation of these compounds and the content of polymeric -CF_x was much higher than LiF. The O 1s peak yielded four components corresponding to Li_2O , C=0, Li_2CO_3 and ROCO_2Li (or) N-O at 528.2, 530.7, 531.8, and 533.5 eV, respectively [50,51]. Since LiNO3 was used as the additive, Li₃N and -NC/-NH groups were also found in the SEI (Fig. S19a). Deconvolution of S 2p peaks revealed the presence of SO₃²⁻ and sulfone groups on the surface and the presence of lithium sulfides in the deeper layers (Fig. S19b) [52,53].

From these deconvoluted high-resolution spectra of C 1s, F 1s, and O 1s peaks, it can be understood that a greater fraction of the topmost layer of the SEI consist of organic compounds such as RCOOLi, Li-O-R, Li-O-R-O-Li, -CF_X, etc., which are formed by the reductive decomposition of solvents and salt. In depth profiling by XPS, a decrease in the organic species accompanied by an increase in the inorganic compounds such as LiF, Li₂O was observed in deeper regions after 60 s of Ar⁺ ion etching. The Li₂CO₃ content, however, remained similar at different depths, indicating its homogeneous distribution throughout the SEI. From these observations, it can be concluded that the SEI consists of mainly an organic matrix whose inner layer is enriched with LiF and Li₂O while Li₂CO₃ homogeneously distributed throughout the matrix. This is consistent with the recent findings in literature where inorganic lithium compounds are found to be embedded in an amorphous polymeric organic matrix [54]. With continuing Ar⁺ etching for 240 s, XPS signals from Ni 2p were detected as shown in Fig. S20. This is an indication that the SEI lying on top of the VACNF arrays are mostly etched off. From this, the thickness of this top SEI layer was calculated to be 19.2 nm based on the Ta_2O_3 calibration standard. Since the composition of SEI is of heterogeneous nature, the actual thickness might be larger due to the higher sputtering yield for soft organic SEI.

If the SEI only exists above the VACNF array, the signals from the SEI components should fade away versus the sputtering time. However, we observed a SEI with a composition resembling that of the inner layer of the SEI located on top of the VACNF array even after etching for 360 s. This observation indicates the existence of a SEI on the sidewall of VACNFs as well. The SEIs on top and side of lithiated VACNFs are designated as top SEI and side SEI, respectively. The organic component of SEI is attributed to incomplete reduction of solvents and salt while their complete reduction leads to inorganic compounds [50]. Taking this into account, the formation of top SEI and side SEI might occur in different stages based on the extent of electrolyte reduction. In the first stage, most of the electrolyte might have been reduced completely which takes place around the sidewall surfaces of VACNFs. This becomes the solid-state barrier for the Li+ ions intercalating into the VACNFs. Simultaneously, another SEI layer might form on top of the VACNF array. In the second stage, the electrolyte reduction is likely incomplete and occurs mostly on top of the VACNF array. With the help of depth profiling by XPS, we were able to reveal the formation of two different SEIs during the Li intercalation into VACNFs.

For Li plated VACNF/Cu, the high-resolution XPS spectra of Ni 2p, C 1s, F 1s, and O 1s of VACNFs after plating with 2.0 mAh/cm² of Li are shown in Fig. S21. The SEI formed on Li plated VACNFs, designated as e-Li SEI, was found to have a mosaic structure similar to that of side SEI of Li-intercalated VACNFs prior to Li plating. Considering the existence of two different types of e-Li as illustrated in Fig. 2, the composition revealed by XPS can be assigned to the SEIs on the top surface of micronscale columnar Li grains as well as the outer sheath around the coaxial nanoscale Li. The 3D nature of e-Li SEI as shown in Fig. 2g-i indicates that, during Li plating, the preformed top and side SEIs are likely transformed into similar compositions which are rich in inorganic compounds. These SEIs consisted of a higher content of inorganic compounds such as Li₂C₂, LiF, Li₂O and Li₂CO₃ compared to the top SEI formed during Li intercalation stage. With the increased depth, these contents increased further. The higher content of inorganic compounds could be attributed to the higher degree of reduction due to its direct contact with e-Li. The heterogeneous 3D structure of the e-Li made it difficult to quantify the thickness of e-Li SEI. Nevertheless, our current study provides the first observation on the complicated SEIs in 3D hosts, which could provide useful guidance for future studies.

3.4.2. Cryo-TEM imaging of VACNFs after lithiation and lithium plating

A cryo-TEM image of a pristine VACNF processed in the same manner as other samples is shown in Fig. 5a revealing that the structure of VACNF is unaffected by the employed sample preparation method (including scraping, washing with the solvent and depositing on TEM grids). It could be observed that the diameter of a pristine VACNF was approximately equal to the widest part of the Ni nanoparticle. Upon lithiation, a co-axial film was observed only at the sidewall of the VACNF, which can be assigned as the side SEI (Fig. 5b). Surprisingly, the top SEI which was unveiled by XPS cannot be found on top of the Ni nanoparticle in the cryo-TEM image. This suggests that the top SEI is likely a continuous self-sustained film which is loosely attached to tips of the VACNF array. It may have been lifted off when the VACNFs were scraped off the Cu substrate during TEM sample preparation. The FE-SEM images of pristine VACNF/Cu (Figs. S22a-S22c) and lithiated VACNF/Cu (Figs. S22e-S22g) prepared by the same method further revealed the presence of nanoscale side SEI film around individual VAC-NFs. The pristine VACNF array collapsed into 1-2 µm wide pyramid shaped bundles as a result of the elastocapillary aggregation caused by the capillary forces during drying of DME solvent following electrode washing. This phenomenon was well documented in our previous work [55-57]. Importantly, our previous work demonstrated that a thin coaxial polymeric coating (down to ~20 nm in thickness) on each VAC-NFs was sufficient to prevent such elastocapillary aggregation [55–57]. Indeed, the lithiated VACNFs in Figs. S22e-S22g were able to retain the vertical array structure without collapsing into microbundles. This further validates the presence of the coaxial side SEI sheath.

Fig. 5c and Fig. S23 reveal the nature of nanoscale e-Li that forms uniformly on the individual VACNFs resulting in the coaxial Li deposition around the entire VACNF surface. The thickness of the nanoscale e-Li and its corresponding SEI were in the range of 10–21 nm and 30–60 nm after plating with 0.75 mAh/cm² and 2.0 mAh/cm², respectively. It is to be noted that these VACNFs observed under TEM are

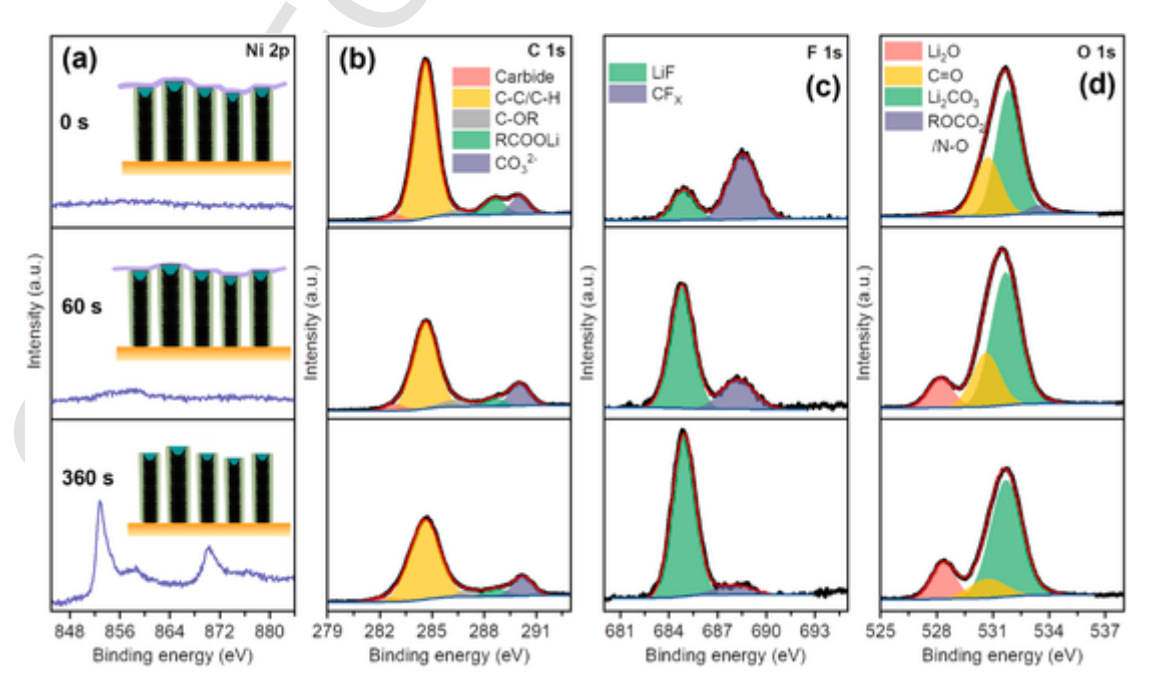


Fig. 4. XPS depth profiling of Li intercalated VACNF/Cu electrode. High-resolution spectra of (a) Ni 2p, (b) C 1s, (c) F 1s, (d) O 1s. Ar^+ ion etching rate is 0.08 nm/s calibrated using Ta_2O_3 . Inset in Fig. 4a shows graphical images to illustrate the depth at which XPS signals were collected. (A colour version of this figure can be viewed online.)

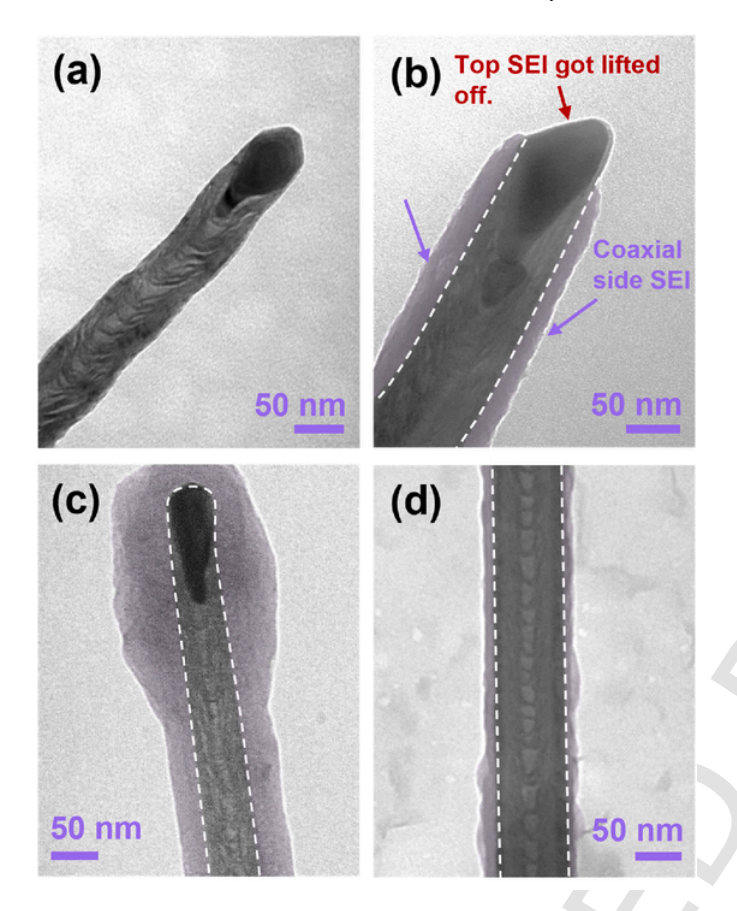


Fig. 5. Cryo-TEM images of VACNFs scraped off from the electrodes (a) in the pristine condition, (b) after Li intercalation, (c) after plating with 2.0 mAh/cm² of Li at 1.0 mA/cm², and (d) after completely stripping of plated Li at 1.0 mA/cm². (A colour version of this figure can be viewed online.)

mostly from the interstitial regions between the infiltrative-Li grains since the VACNFs in later ones are embedded inside Li grains and are not easy to be broken free. Most of the growth of nanoscale e-Li seems to occur in the later part of plating step and some nanoscale e-Li still exists even after plating a capacity of 2.0 mAh/cm², which are consistent with the FESEM results in Fig. 2b-c. In contrast to the Li-intercalated sample, the tip of Li-plated VACNFs was covered by Li metal and e-Li SEI. The coaxial Li deposition is favored for suppressing dendrite growth, which may be enhanced by further improving lithiophilicity in our future studies [47]. The SAED pattern in Fig. S24 shows the amorphous nature of nanoscale e-Li on VACNFs. It was reported that, at low current densities, Li was normally electrodeposited as amorphous "glassy" Li [58], which was favored for stable and reversible Li plating/ stripping. The high surface area provided by the VACNFs results in a low local current density which faciliates the formation of the amorphous Li. During subsequent stripping of the e-Li, the thickness of the coaxial film around the VACNFs was reduced as shown in Fig. 5d. Since the formation of SEI is irreversible, the coaxial film on Li-stripped VAC-NFs can be assigned to the SEI of nanoscale e-Li. Fig. S25 shows that the coaxial SEI after Li stripping bulged into a small bubble due to the heating by the prolonged electron beam exposure, which further confirms its coaxial and elastic nature. The difference in the appearance between the side SEI preformed around VACNFs and the later SEI on the coaxial nanoscale e-Li confirms the transformation of preformed SEIs at intercalation stage into chemically distinct e-Li SEI (richer with inorganic components) as shown in Fig. S21.

The insights gained so far are schematically illustrated in Fig. 6. XPS and cryo-TEM measurements revealed the existence of two different types of SEIs during the Li intercalation stage, including (i) top SEI and

(ii) side SEI. The top SEI is rich in organic moieties due to incomplete decomposition of electrolyte while the side SEI is rich in inorganic lithium compounds. The top SEI blankets the VACNFs array while the side SEI forms a coaxial sheath uniformly wrapping the individual VAC-NFs. Spectroscopic data from in-situ Raman and electrochemical data showed that the outer layer of VACNFs were lithiated, making it lithiophilic that favored the lithium nucleation in the following Li electrodeposition. The lithiation and delithiation processes occur reversibly without damaging the structural integrity. During Li plating, e-Li grows into two different morphologies, (i) infiltrative e-Li and (ii) nanoscale e-Li, along with the formation of a new SEI on the e-Li surface that is rich with inorganic lithium compounds. Infiltrative e-Li exhibits a dense, non-porous, micron-scale columnar structure infiltrating the pore volume between VACNFs. A small amount of e-Li exists in the interstitial area between the infiltrative e-Li grains, as nanoscale Li deposits coaxially around individual VACNFs. During Li stripping, the infiltrative e-Li leaves behind irreversible SEI skins loosely attached to the VACNF arrays. The SEI of nanoscale e-Li is also rich with inorganic compounds but behaves as a stable elastic sheath coaxially wrapped around individual VACNFs.

3.5. FESEM imaging of VACNF/Cu after Li plating/stripping cycling

The morphology of VACNF/Cu electrodes after Li plating/stripping cycling was studied using FESEM. Due to the irreversible and dynamic nature, a large amount of infiltrative e-Li's SEI skins formed in preceding stripping cycles accumulated on top of the VACNF arrays (Fig. S26). As shown in Figs. S27a-S27c, at the end of 50 cycles, the e-Li's SEI completely covered the top surface of VACNF/Cu electrode. The accumulated SEI skins are likely dominated by the e-Li SEI that broke off from the electrode during Li stripping. The irreversible shedding of SEI skins not only consumes electrolyte, but also affects the accessibility of graphitic edges of VACNFs for Li nucleation in the subsequent cycles and increases the tortuosity of the electrode [59]. This is well reflected in the electrochemical performance where an increase in the Li plating/ stripping overpotential was observed towards the end of the cycle life. In comparison, even thicker layers of dead Li mixed with SEI skins were observed in cycled planar Cu electrodes (Figs. S27d-S27f). Continuous consumption of lithium nitrate additive and its effect on morphology of lithium were also observed [60,61]. These led to the highly nonuniform optical image in Fig. S27d. It can be concluded that accumulation of dead Li and SEI and electrolyte consumption were the primary reasons for the failure of planar Cu electrodes. These are reduced but not eliminated in 3D nanostructured electrodes such as VACNF arrays. Further studies to quantify SEI and dead Li, and understand their evolution are necessary to develop mitigation solutions. Nevertheless, a common observation of both cycled VACNF/Cu and planar Cu electrodes is the high degree of multiscale heterogeneity in both SEIs and Li deposits. Development of 3D host structures that can facilitate formation of stable SEIs is critical for commercialization of Li metal anodes.

4. Conclusion

VACNF array electrodes are employed as a model 3D conductive host to understand the critical issues toward future LMAs. The fundamental issues, such as the structure of SEI and the morphological evolution of Li deposition, during the lithium plating/stripping processes were studied with various spectroscopic and microscopic techniques. At electrode potentials positive to Li⁺/Li, lithium intercalation and deintercalation occur at the VACNF sidewall in a reversible manner without disrupting its structure. The lithiation makes the VACNFs more lithiophilic which favors subsequent lithium plating. During electrodeposition onto the VACNF/Cu electrode, lithium grows into two different morphologies - the micron-scale columnar infiltrative Li and the nanoscale coaxial Li sheath. Reversible lithiation/delithiation and Li

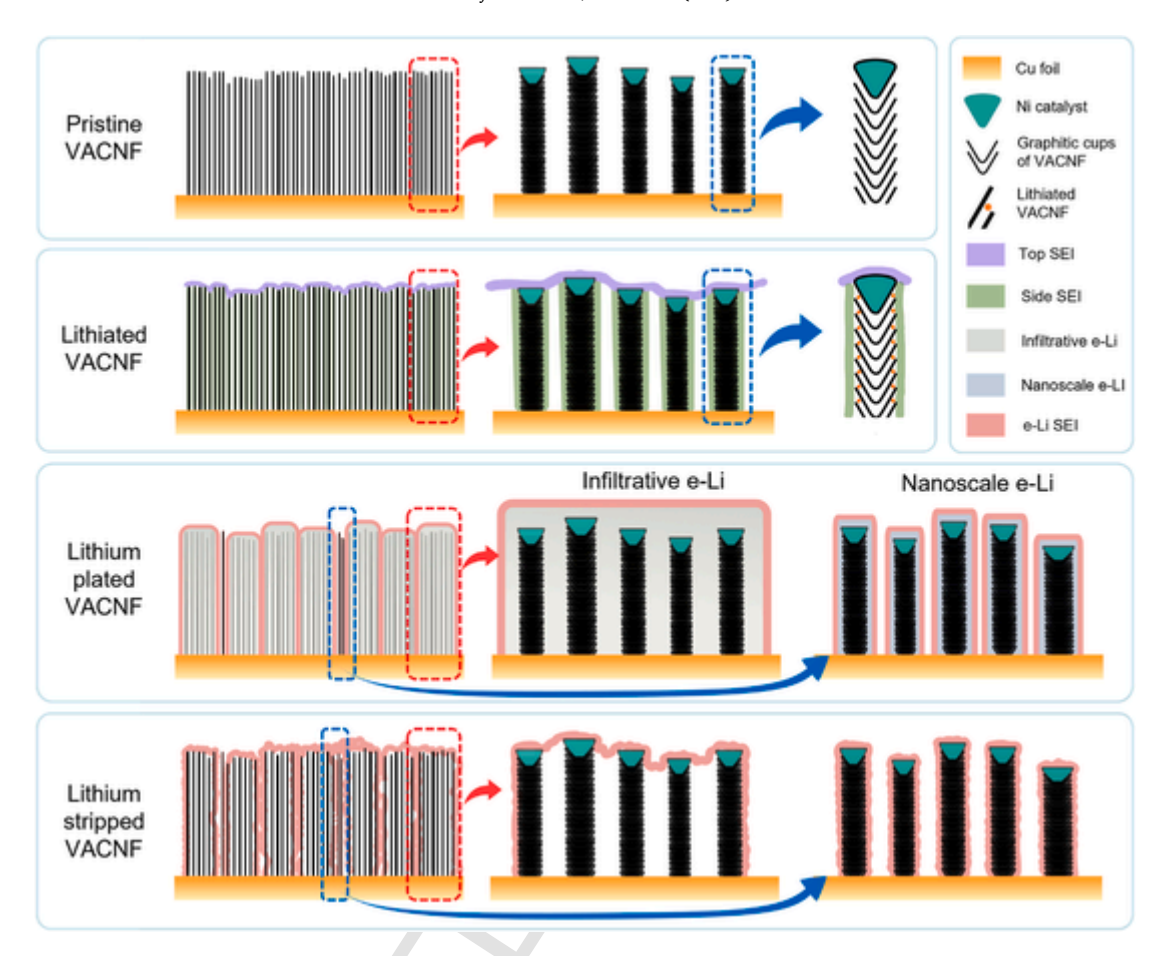


Fig. 6. Schematic to illustrate the structure of SEI formed during Li intercalation, Li plating/stripping and the morphology of electrodeposited Li on VACNF/Cu electrode. (A colour version of this figure can be viewed online.)

plating/stripping were observed in situ based on the D and G bands of graphitic carbon and the Raman band of lithium acetylide/carbide (Li₂C₂), respectively. The high performance of VACNF/Cu as a LMA host is attributed to the combination of the low surface area of solid infiltrative Li grains and the stable SEI on the surface of nanoscale Li. Depth-profiling XPS revealed the formation of two types of SEIs at the Li intercalation stage, i.e., a continuous organic-rich SEI film loosely attached to the top surface of the VACNF array and an inorganic-rich coaxial SEI sheath around individual VACNFs. During Li plating, they were both transformed into an inorganic-rich SEI directly on the surface of the electrodeposited lithium. After stripping Li, soft SEI skins from the infiltrative Li grains were left loosely on the VACNF array and accumulated during cycling while the coaxial SEI on the nanoscale Li remained as a stable elastic sheath. The loose SEI skins were the main factor for electrolyte consumption and increased heterogeneity, eventually leading to cell failure. Though 3D hosts enhance the performance of LMAs proving to be a promising route for suppressing dendrite formation, other challenges, such as continuous electrolyte consumption, need to be overcome. Further developments including host structure design, surface modification and electrolyte additive optimization are needed to improve the uniformity of lithium nucleation and to achieve stable, robust SEIs during cycling. These are essential to realize viable 3D LMAs. These results provide useful insights to guide the future design and development of 3D host structures for long-life LMAs. For 3D hosts similar to VACNF/Cu, application of preformed artificial SEIs or in-situ formed SEIs with high Li+ conductivity and mechanical/chemical stability during cycling needs to be further studied to develop better solutions. Other approaches such as enhanced lithiophilicity by surface treatment might also be adopted for similar low tortuous 3D hosts towards high performance LMAs.

CRediT authorship contribution statement

Sabari Rajendran : Conceptualization, Formal analysis, Investigation, Methodology, Validation, Visualization, Writing – original draft. **Archana Sekar :** Formal analysis, Writing – review & editing. **Jun Li :** Conceptualization, Formal analysis, Funding acquisition, Methodology, Project administration, Resources, Supervision, Writing – review & editing.

Declaration of competing interest

The authors declare that they have no known competing financial interests or personal relationships that could have appeared to influence the work reported in this paper.

Acknowledgement

This work was supported by the US National Science Foundation grants CBET-2054754 and DMR-1707585. We would like to thank Dr. Balasubramanian Balamurugan from the University of Nebraska for the XPS measurements and Dr. Dan Boyle at the Kansas State University Microscopy Facility in the Division of Biology for help in cryo-TEM imaging. The XPS and FIB-FESEM characterizations were performed in the Nebraska Nanoscale Facility: National Nanotechnology Coordinated Infrastructure and the Nebraska Center for Materials and Nanoscience

(and/or NERCF), which are supported by the National Science Foundation under Award ECCS: 2025298 and the Nebraska Research Initiative.

Appendix A. Supplementary data

Supplementary data to this article can be found online at https://doi.org/10.1016/j.carbon.2023.118174.

References

- P.G. Bruce, S.A. Freunberger, L.J. Hardwick, J.-M. Tarascon, Li-O 2 and Li-S batteries with high energy storage, Nat. Mater. 11 (2012) 19–29, https://doi.org/ 10.1038/nmat3191.
- [2] W. Xu, J. Wang, F. Ding, X. Chen, E. Nasybulin, Y. Zhang, J.-G. Zhang, Lithium metal anodes for rechargeable batteries, Energy Environ. Sci. 7 (2014) 513–537, https://doi.org/10.1039/C3EE40795K.
- [3] D. Lin, Y. Liu, Y. Cui, Reviving the lithium metal anode for high-energy batteries, Nat. Nanotechnol. 12 (2017) 194–206, https://doi.org/10.1038/nnano.2017.16.
- [4] J. Zheng, T. Tang, Q. Zhao, X. Liu, Y. Deng, L.A. Archer, Physical orphaning versus chemical instability: is dendritic electrodeposition of Li fatal? ACS Energy Lett. 4 (2019) 1349–1355, https://doi.org/10.1021/acsenergylett.9b00750.
- [5] Z.A. Ghazi, Z. Sun, C. Sun, F. Qi, B. An, F. Li, H.-M. Cheng, Key aspects of lithium metal anodes for lithium metal batteries, Small 15 (2019) 1900687, https:// doi.org/10.1002/smll.201900687.
- [6] A. Aryanfar, D.J. Brooks, A.J. Colussi, M.R. Hoffmann, Quantifying the dependence of dead lithium losses on the cycling period in lithium metal batteries, Phys. Chem. Chem. Phys. 16 (2014) 24965–24970, https://doi.org/10.1039/ C4CP03590A.
- [7] K.L. Jungjohann, R.N. Gannon, S. Goriparti, S.J. Randolph, L.C. Merrill, D.C. Johnson, K.R. Zavadil, S.J. Harris, K.L. Harrison, Cryogenic laser ablation reveals short-circuit mechanism in lithium metal batteries, ACS Energy Lett. 6 (2021) 2138–2144, https://doi.org/10.1021/acsenergylett.1c00509.
- [8] C.-P. Yang, Y.-X. Yin, S.-F. Zhang, N.-W. Li, Y.-G. Guo, Accommodating lithium into 3D current collectors with a submicron skeleton towards long-life lithium metal anodes, Nat. Commun. 6 (2015) 8058, https://doi.org/10.1038/ ncomms9058.
- [9] F. Ding, W. Xu, G.L. Graff, J. Zhang, M.L. Sushko, X. Chen, Y. Shao, M.H. Engelhard, Z. Nie, J. Xiao, X. Liu, P.V. Sushko, J. Liu, J.-G. Zhang, Dendrite-Free lithium deposition via self-healing electrostatic shield mechanism, J. Am. Chem. Soc. 135 (2013) 4450–4456, https://doi.org/10.1021/ja312241y.
- [10] J. Heine, P. Hilbig, X. Qi, P. Niehoff, M. Winter, P. Bieker, Fluoroethylene carbonate as electrolyte additive in tetraethylene glycol dimethyl ether based electrolytes for application in lithium ion and lithium metal batteries, J. Electrochem. Soc. 162 (2015) A1094, https://doi.org/10.1149/2.0011507jes.
- [11] E. Kazyak, K.N. Wood, N.P. Dasgupta, Improved cycle life and stability of lithium metal anodes through ultrathin atomic layer deposition surface treatments, Chem. Mater. 27 (2015) 6457–6462, https://doi.org/10.1021/acs.chemmater.5b02789.
- [12] C. Wang, Y. Yang, X. Liu, H. Zhong, H. Xu, Z. Xu, H. Shao, F. Ding, Suppression of lithium dendrite formation by using LAGP-PEO (LiTFSI) composite solid electrolyte and lithium metal anode modified by PEO (LiTFSI) in all-solid-state lithium batteries, ACS Appl. Mater. Interfaces 9 (2017) 13694–13702, https://doi.org/ 10.1021/acsami.7b00336.
- Y. Chen, A. Elangovan, D. Zeng, Y. Zhang, H. Ke, J. Li, Y. Sun, H. Cheng, Vertically aligned carbon nanofibers on Cu foil as a 3D current collector for reversible Li plating/stripping toward high-performance Li–S batteries, Adv. Funct. Mater. 30 (2020) 1906444, https://doi.org/10.1002/adfm.201906444.
 X.-R. Chen, C. Yan, J.-F. Ding, H.-J. Peng, Q. Zhang, New insights into "dead
- [14] X.-R. Chen, C. Yan, J.-F. Ding, H.-J. Peng, Q. Zhang, New insights into "dead lithium" during stripping in lithium metal batteries, J. Energy Chem. 62 (2021) 289–294, https://doi.org/10.1016/j.jechem.2021.03.048.
- [15] Y. Cheng, J. Chen, Y. Chen, X. Ke, J. Li, Y. Yang, Z. Shi, Lithium Host: Advanced architecture components for lithium metal anode, Energy Storage Mater. 38 (2021) 276–298, https://doi.org/10.1016/j.ensm.2021.03.008.
- [16] X. Yan, L. Lin, Q. Chen, Q. Xie, B. Qu, L. Wang, D.-L. Peng, Multifunctional roles of carbon-based hosts for Li-metal anodes: a review, Carbon Energy 3 (2021) 303–329, https://doi.org/10.1002/cey2.95.
- [17] X. Chen, X.-R. Chen, T.-Z. Hou, B.-Q. Li, X.-B. Cheng, R. Zhang, Q. Zhang, Lithiophilicity chemistry of heteroatom-doped carbon to guide uniform lithium nucleation in lithium metal anodes, Sci. Adv. 5 (2019) eaau7728, https://doi.org/ 10.1126/sciady.aau7728.
- [18] J. Wang, H. Wang, J. Xie, A. Yang, A. Pei, C.-L. Wu, F. Shi, Y. Liu, D. Lin, Y. Gong, Y. Cui, Fundamental study on the wetting property of liquid lithium, Energy Storage Mater. 14 (2018) 345–350, https://doi.org/10.1016/j.ensm.2018.05.021.
- [19] X. Zhao, S. Xia, X. Zhang, Y. Pang, F. Xu, J. Yang, L. Sun, S. Zheng, Highly lithiophilic copper-reinforced scaffold enables stable Li metal anode, ACS Appl. Mater. Interfaces 13 (2021) 20240–20250, https://doi.org/10.1021/ acsami.1c04735.
- [20] Y. Fang, S.L. Zhang, Z.-P. Wu, D. Luan, X.W. David Lou, A highly stable lithium metal anode enabled by Ag nanoparticle–embedded nitrogen-doped carbon macroporous fibers, Sci. Adv. 7 (2021) eabg3626, https://doi.org/10.1126/ sciadv.abe3626.
- [21] D. Li, C. Xie, Y. Gao, H. Hu, L. Wang, Z. Zheng, Inverted anode structure for long-life lithium metal batteries, Adv. Energy Mater. 12 (2022) 2200584, https://doi.org/10.1002/aenm.202200584.

- [22] Y. Shi, B. Li, Y. Zhang, Y. Cui, Z. Cao, Z. Du, J. Gu, K. Shen, S. Yang, Tortuosity modulation toward high-energy and high-power lithium metal batteries, Adv. Energy Mater. (2021) 2003663, https://doi.org/10.1002/aenm.202003663.
- [23] W. Deng, W. Zhu, X. Zhou, X. Peng, Z. Liu, Highly reversible Li plating confined in three-dimensional interconnected microchannels toward high-rate and stable metallic lithium anodes, ACS Appl. Mater. Interfaces 10 (2018) 20387–20395, https://doi.org/10.1021/acsami.8b02619.
- [24] Y. Zhang, W. Luo, C. Wang, Y. Li, C. Chen, J. Song, J. Dai, E.M. Hitz, S. Xu, C. Yang, Y. Wang, L. Hu, High-capacity, low-tortuosity, and channel-guided lithium metal anode, Proc. Natl. Acad. Sci. USA 114 (2017) 3584–3589, https://doi.org/10.1073/pnas.1618871114.
- [25] D. Lin, Y. Liu, Z. Liang, H.-W. Lee, J. Sun, H. Wang, K. Yan, J. Xie, Y. Cui, Layered reduced graphene oxide with nanoscale interlayer gaps as a stable host for lithium metal anodes, Nat. Nanotechnol. 11 (2016) 626–632, https://doi.org/10.1038/ nnano.2016.32.
- [26] H. Li, D. Chao, B. Chen, X. Chen, C. Chuah, Y. Tang, Y. Jiao, M. Jaroniec, S.-Z. Qiao, Revealing principles for design of lean-electrolyte lithium metal anode via in situ spectroscopy, J. Am. Chem. Soc. 142 (2020) 2012–2022, https://doi.org/10.1021/jacs.9b11774.
- [27] R. Zhang, X.-R. Chen, X. Chen, X.-B. Cheng, X.-Q. Zhang, C. Yan, Q. Zhang, Lithiophilic sites in doped graphene guide uniform lithium nucleation for dendritefree lithium metal anodes, Angew. Chem. Int. Ed. 56 (2017) 7764–7768, https:// doi.org/10.1002/anie.201702099.
- [28] Y.-X. Zhan, P. Shi, X.-Q. Zhang, F. Ding, J.-Q. Huang, Z. Jin, R. Xiang, X. Liu, Q. Zhang, The insights of lithium metal plating/stripping in porous hosts: progress and perspectives, Energy Technol. 9 (2021) 2000700, https://doi.org/10.1002/ente.202000700.
- [29] S.A. Klankowski, R.A. Rojeski, B.A. Cruden, J. Liu, J. Wu, J. Li, A high-performance lithium-ion battery anode based on the core-shell heterostructure of silicon-coated vertically aligned carbon nanofibers, J. Mater. Chem. 1 (2013) 1055–1064, https://doi.org/10.1039/C2TA00057A.
- [30] S.A. Klankowski, G.P. Pandey, B.A. Cruden, J. Liu, J. Wu, R.A. Rojeski, J. Li, Anomalous capacity increase at high-rates in lithium-ion battery anodes based on silicon-coated vertically aligned carbon nanofibers, J. Power Sources 276 (2015) 73–79, https://doi.org/10.1016/j.jpowsour.2014.11.094.
- [31] Z. Zhang, J. Wang, X. Yan, S. Zhang, W. Yang, Z. Zhuang, W.-Q. Han, In-situ growth of hierarchical N-doped CNTs/Ni Foam scaffold for dendrite-free lithium metal anode, Energy Storage Mater. 29 (2020) 332–340, https://doi.org/10.1016/ j.ensm.2020.04.022.
- [32] J. Liu, J. Essner, J. Li, Hybrid supercapacitor based on coaxially coated manganese oxide on vertically aligned carbon nanofiber arrays, Chem. Mater. 22 (2010) 5022–5030, https://doi.org/10.1021/cm101591p.
- [33] X. Shen, X.-Q. Zhang, F. Ding, J.-Q. Huang, R. Xu, X. Chen, C. Yan, F.-Y. Su, C.-M. Chen, X. Liu, Q. Zhang, Advanced electrode materials in lithium batteries: retrospect and prospect, Energy Mater. Adv. 2021 (2021) https://doi.org/10.34133/2021/1205324, 2021/1205324.
- [34] Y. An, Y. Tian, Y. Li, C. Wei, Y. Tao, Y. Liu, B. Xi, S. Xiong, J. Feng, Y. Qian, Heteroatom-doped 3D porous carbon architectures for highly stable aqueous zinc metal batteries and non-aqueous lithium metal batteries, Chem. Eng. J. 400 (2020) 125843, https://doi.org/10.1016/j.cej.2020.125843.
- [35] H. Chen, A. Pei, J. Wan, D. Lin, R. Vilá, H. Wang, D. Mackanic, H.-G. Steinrück, W. Huang, Y. Li, A. Yang, J. Xie, Y. Wu, H. Wang, Y. Cui, Tortuosity effects in lithium-metal host anodes, Joule 4 (2020) 938–952, https://doi.org/10.1016/j.joule.2020.03.008.
- [36] F. Liu, R. Xu, Y. Wu, D.T. Boyle, A. Yang, J. Xu, Y. Zhu, Y. Ye, Z. Yu, Z. Zhang, X. Xiao, W. Huang, H. Wang, H. Chen, Y. Cui, Dynamic spatial progression of isolated lithium during battery operations, Nature 600 (2021) 659–663, https://doi.org/10.1038/s41586-021-04168-w.
- [37] K.-H. Chen, K.N. Wood, E. Kazyak, W.S. LePage, A.L. Davis, A.J. Sanchez, N.P. Dasgupta, Dead lithium: mass transport effects on voltage, capacity, and failure of lithium metal anodes, J. Mater. Chem. 5 (2017) 11671–11681, https://doi.org/10.1039/C7TA00371D.
- [38] Q. Ma, X. Zhang, A. Wang, Y. Xia, X. Liu, J. Luo, Stabilizing solid electrolyte interphases on both anode and cathode for high areal capacity, high-voltage lithium metal batteries with high Li utilization and lean electrolyte, Adv. Funct. Mater. 30 (2020) 2002824, https://doi.org/10.1002/adfm.202002824.
- [39] Y. Yang, Y. Yin, D.M. Davies, M. Zhang, M. Mayer, Liquefied gas electrolytes for wide-temperature lithium metal batteries, Environ. Sci.. ((n.d.)).
- [40] C. Fang, J. Li, M. Zhang, Y. Zhang, F. Yang, J.Z. Lee, M.-H. Lee, J. Alvarado, M.A. Schroeder, Y. Yang, B. Lu, N. Williams, M. Ceja, L. Yang, M. Cai, J. Gu, K. Xu, X. Wang, Y.S. Meng, Quantifying inactive lithium in lithium metal batteries, Nature 572 (2019) 511–515, https://doi.org/10.1038/s41586-019-1481-z.
- [41] A. Pei, G. Zheng, F. Shi, Y. Li, Y. Cui, Nanoscale nucleation and growth of electrodeposited lithium metal, Nano Lett. 17 (2017) 1132–1139, https://doi.org/ 10.1021/acs.nanolett.6b04755.
- [42] S.H. Park, Y.J. Lee, Morphological control of electrodeposited lithium metal via seeded growth: stepwise spherical to fibrous lithium growth, J. Mater. Chem. A. 9 (2021) 1803–1811, https://doi.org/10.1039/D0TA10006D.
- [43] F.-N. Jiang, S.-J. Yang, H. Liu, X.-B. Cheng, L. Liu, R. Xiang, Q. Zhang, S. Kaskel, J.-Q. Huang, Mechanism understanding for stripping electrochemistry of Li metal anode, SusMat 1 (2021) 506–536, https://doi.org/10.1002/sus2.37.
- [44] M.-T. Fonseca Rodrigues, V.A. Maroni, D.J. Gosztola, K.P.C. Yao, K. Kalaga, I.A. Shkrob, D.P. Abraham, Lithium acetylide: a spectroscopic marker for lithium deposition during fast charging of Li-ion cells, ACS Appl. Energy Mater. 2 (2019) 873–881, https://doi.org/10.1021/acsaem.8b01975.
- [45] S. Migge, G. Sandmann, D. Rahner, H. Dietz, W. Plieth, Studying lithium

- intercalation into graphite particles via in situ Raman spectroscopy and confocal microscopy, J. Solid State Electrochem. 9 (2005) 132–137, https://doi.org/10.1007/s10008-004-0563-4
- [46] W. Bao, J. Wan, X. Han, X. Cai, H. Zhu, D. Kim, D. Ma, Y. Xu, J.N. Munday, H.D. Drew, M.S. Fuhrer, L. Hu, Approaching the limits of transparency and conductivity in graphitic materials through lithium intercalation, Nat. Commun. 5 (2014) 4224, https://doi.org/10.1038/ncomms5224.
- [47] P. Shi, T. Li, R. Zhang, X. Shen, X.-B. Cheng, R. Xu, J.-Q. Huang, X.-R. Chen, H. Liu, Q. Zhang, Lithiophilic LiC6 layers on carbon hosts enabling stable Li metal anode in working batteries, Adv. Mater. 31 (2019) 1807131, https://doi.org/10.1002/adma.201807131.
- [48] J.J. Lodico, M. Woodall, H.L. Chan, W.A. Hubbard, B.C. Regan, In situ optical microscopy of the electrochemical intercalation of lithium into single crystal graphite, Microsc. Microanal. 23 (2017) 1982–1983, https://doi.org/10.1017/ S1431927617010571.
- [49] B. von Holtum, M. Kubot, C. Peschel, U. Rodehorst, M. Winter, S. Nowak, S. Wiemers-Meyer, Accessing the Primary Solid–Electrolyte Interphase on Lithium Metal: A Method for Low-Concentration Compound Analysis, ChemSusChem. n/a (n.d.) e202201912. https://doi.org/10.1002/cssc.202201912.
- [50] Q. Liu, A. Cresce, M. Schroeder, K. Xu, D. Mu, B. Wu, L. Shi, F. Wu, Insight on lithium metal anode interphasial chemistry: reduction mechanism of cyclic ether solvent and SEI film formation, Energy Storage Mater. 17 (2019) 366–373, https:// doi.org/10.1016/j.ensm.2018.09.024.
- [51] T. Jaumann, J. Balach, M. Klose, S. Oswald, J. Eckert, L. Giebeler, Role of 1,3-dioxolane and LiNO3 addition on the long term stability of nanostructured silicon/carbon anodes for rechargeable lithium batteries, J. Electrochem. Soc. 163 (2016) A557, https://doi.org/10.1149/2.1011603jes.
- [52] Y. Wang, C.-F. Lin, J. Rao, K. Gaskell, G. Rubloff, S.B. Lee, Electrochemically controlled solid electrolyte interphase layers enable superior Li–S batteries, ACS Appl. Mater. Interfaces 10 (2018) 24554–24563, https://doi.org/10.1021/ acsami.8b07248.
- [53] W. Li, H. Yao, K. Yan, G. Zheng, Z. Liang, Y.-M. Chiang, Y. Cui, The synergetic

- effect of lithium polysulfide and lithium nitrate to prevent lithium dendrite growth, Nat. Commun. 6 (2015) 7436, https://doi.org/10.1038/ncomms8436.
- [54] B. Han, X. Li, S. Bai, Y. Zou, B. Lu, M. Zhang, X. Ma, Z. Chang, Y.S. Meng, M. Gu, Conformal three-dimensional interphase of Li metal anode revealed by low-dose cryoelectron microscopy, Matter 4 (2021) 3741–3752, https://doi.org/10.1016/ i_matt_2021_09_019
- [55] T.D.B. Nguyen-Vu, H. Chen, A.M. Cassell, R.J. Andrews, M. Meyyappan, J. Li, Vertically aligned carbon nanofiber architecture as a multifunctional 3-D neural electrical interface, IEEE (Inst. Electr. Electron. Eng.) Trans. Biomed. Eng. 54 (2007) 1121–1128, https://doi.org/10.1109/TBME.2007.891169.
- [56] E.D. de Asis, T.D.B. Nguyen-Vu, P.U. Arumugam, H. Chen, A.M. Cassell, R.J. Andrews, C.Y. Yang, J. Li, High efficient electrical stimulation of hippocampal slices with vertically aligned carbon nanofiber microbrush array, Biomed. Microdevices 11 (2009) 801–808, https://doi.org/10.1007/s10544-009-9295-7
- [57] T.D.B. Nguyen-Vu, H. Chen, A.M. Cassell, R. Andrews, M. Meyyappan, J. Li, Vertically aligned carbon nanofiber arrays: an advance toward electrical–neural interfaces, Small 2 (2006) 89–94, https://doi.org/10.1002/smll.200500175.
- [58] X. Wang, G. Pawar, Y. Li, X. Ren, M. Zhang, B. Lu, A. Banerjee, P. Liu, E.J. Dufek, J.-G. Zhang, J. Xiao, J. Liu, Y.S. Meng, B. Liaw, Glassy Li metal anode for highperformance rechargeable Li batteries, Nat. Mater. (2020) 1–7, https://doi.org/ 10.1038/s41563-020-0729-1.
- [59] Y.-X. Zhan, P. Shi, X.-X. Ma, C.-B. Jin, Q.-K. Zhang, S.-J. Yang, B.-Q. Li, X.-Q. Zhang, J.-Q. Huang, Failure mechanism of lithiophilic sites in composite lithium metal anode under practical conditions, Adv. Energy Mater. 12 (2022) 2103291, https://doi.org/10.1002/aenm.202103291.
- [60] B.D. Adams, E.V. Carino, J.G. Connell, K.S. Han, R. Cao, J. Chen, J. Zheng, Q. Li, K.T. Mueller, W.A. Henderson, J.-G. Zhang, Long term stability of Li-S batteries using high concentration lithium nitrate electrolytes, Nano Energy 40 (2017) 607–617, https://doi.org/10.1016/j.nanoen.2017.09.015.
- [61] F. Shi, A. Pei, A. Vailionis, J. Xie, B. Liu, J. Zhao, Y. Gong, Y. Cui, Strong texturing of lithium metal in batteries, Proc. Natl. Acad. Sci. USA 114 (2017) 12138–12143, https://doi.org/10.1073/pnas.1708224114.